Se Inter-Diffusion Limits Absorber Layer Grain Growth in CdSe-CdTe Photovoltaics

T.F.S. Altamimi[1], J.F. Leaver[2], K. Durose,[2] J.D. Major,[2] and B.G. Mendis[1,*]

[1]*Department of Physics, Durham University, South Road, Durham, DH1 3LE, United Kingdom*

[2]*Department of Physics, Stephenson Institute for Renewable Energy, University of Liverpool, Liverpool, L69 7ZF, United Kingdom*

Diffusion of Se from the CdSe window layer into the CdTe absorber improves the short circuit current density by narrowing the band gap and increasing the carrier lifetime. Thicker CdSe layers, however, show a dramatic loss in photocurrent collection due to Se over-alloying. Electron microscopy investigations show that this decrease in performance is due to the formation of small grains ($\sim$783 nm average diameter), which exhibit grain boundary porosity in the Se inter-diffusion region. The larger grain boundary area and void free surfaces give rise to higher levels of nonradiative recombination, and therefore, a lower photocurrent. It is proposed that the small grain size is due to a drag force exerted by segregated Se solute atoms on a moving grain boundary, while faster Se diffusion along the grain boundaries results in vacancy build up and porosity due to the Kirkendall effect. The results indicate that the device processing conditions must be carefully controlled such that the negative effects of Se alloying (i.e., smaller grains, Kirkendall voids) do not undermine its benefits.

I. INTRODUCTION

Selenium grading of the absorber layer together with chlorine activation has increased the record cell efficiency of CdTe-based thin-film photovoltaics to 22.4% [1]. There are two ways to achieve a Se composition gradient, namely, co-deposition from CdTe + Se or Cd(Se, Te) ternary sources [2], and sequential deposition of CdSe and CdTe layers [3]. For the latter, Se diffusion creates a $CdSe_xTe_{1-x}$ (CST) inter-mixed layer [3,4]. For clarity, these two device structures are referred to as co-deposited and CdSe-CdTe devices, respectively. Selenium can impact device efficiency in a number of ways. Band gap narrowing [5] in Se alloyed CdTe increases the wavelength spectrum for photocurrent generation, thereby improving the short circuit current density [6,7]. Se also increases the carrier lifetime [8–10], by suppressing nonradiative recombination within the grain interiors of the absorber layer [11], so that the open circuit voltage is similar to CdTe, despite the smaller band gap. Furthermore, cathodoluminescence (CL) imaging indicates lower contrast at CST grain boundaries compared to CdTe [10, 12], suggesting that Se passivates the absorber layer grain boundaries. This was corroborated by density functional theory (DFT) simulations, which reported Se passivation [13] and Se and Cl co-passivation [14], although in another study the segregation energy of Se was too low to passivate the dangling bonds at the grain boundary [15].

Here, we use CL and transmission electron microscopy (TEM) to show that fast inter-diffusion of Se along grain boundaries [16] in CdSe-CdTe photovoltaic devices can limit grain growth and cause grain boundary porosity, provided the Se concentration is sufficiently high. This is a combination of two effects, namely, solute drag of the migrating grain boundary [17,18] and grain boundary Kirkendall voiding [19]. The larger grain boundary area and void free surfaces increase nonradiative carrier recombination in the diffusion zone, leading to lower efficiency devices. This contrasts with high efficiency co-deposited devices, where nonradiative recombination is lower in the CST layer [8,9,11]. Our results suggests that there are limits to absorber layer Se grading that can be achieved through inter-diffusion without compromising device performance. Data reported in the literature [9,11] also show similar effects in co-deposited devices, albeit to a lesser extent. The results reported here are therefore believed to be an intrinsic feature of Se alloying, the magnitude of which is governed by the device processing conditions.

---

*Corresponding author: b.g.mendis@durham.ac.uk

II. EXPERIMENTAL METHODS

Fabrication of the CdSe-CdTe devices was previously reported in Ref. [20]. CdSe layers of variable thickness (i.e., 50, 100, 200, and 400 nm) were deposited by rf sputtering on NSG Ltd. TEC15 soda lime glass. The samples were then held in the close space sublimation (CSS) chamber at 400 Torr base pressure for 20 min before CdTe deposition at 5 Torr pressure. The source and substrate temperatures throughout were 600 and 550 °C, respectively. For chlorine activation, the as-deposited absorber layer was spray coated with a 1 mol/dm^3 aqueous MgCl$_2$ solution and annealed in air at 430 °C for 60 min. 50 nm × 0.24 cm^2 Au back contacts were evaporated through a mask to complete the devices. Samples underwent a 15 s etch in a solution of 1% v/v nitric acid and 70% v/v phosphoric acid, both directly before chlorine activation and directly before back contact deposition. Current-voltage measurements were performed using a TS Space Systems solar simulator and AM1.5 spectrum (1000 W/m^2). A Bentham PVE 300 system was used for external quantum efficiency (EQE) measurements.

Device cross sections for electron microscopy were prepared using a dual-beam Helios 600 focused ion-beam microscope (FIB). Trenches were milled using a 30 kV Ga ion beam, followed by 5 kV ion-beam polishing of the cross-section surface, which had a shallow angle of 8° with respect to the CdTe back surface. These so-called "bevel" cross sections make it easier to characterize inter-diffusion in thin-film devices [11], since the microstructure is elongated in the layer thickness direction (see Fig. 1). The method was used previously for grain size analysis [21] and inter-diffusion profiling [22,23] in CdS-CdTe thin-film photovoltaics. A platinum layer was FIB deposited on the CdTe back surface prior to milling, to reduce the "curtaining" artefact caused by variations in the sputter rate across a rough surface [24]. Electron backscattered diffraction (EBSD) analysis of the bevel cross sections was performed in the Helios 600 FIB at 30 kV electron beam voltage using an Oxford Nordlys detector. CL imaging and spectroscopy were carried out in a Hitachi SU70 scanning electron microscope (SEM) equipped with a Gatan MonoCL system; the electron beam voltage was either 15 or 20 kV. All CL data were acquired at room temperature. Cross sections for TEM were prepared using FIB [24] and examined in a JEOL 2100F field emission gun TEM operating at 200 kV. Spatially resolved chemical analysis was performed in scanning TEM (STEM) mode using an Oxford Instruments X-Max 65T silicon drift detector.

III. RESULTS AND DISCUSSION

EQE results for devices with different CdSe layer thicknesses are shown in Fig. 2(a). The EQE plot for a given CdSe thickness corresponds to the device with highest cell efficiency. Increasing the CdSe layer thickness up
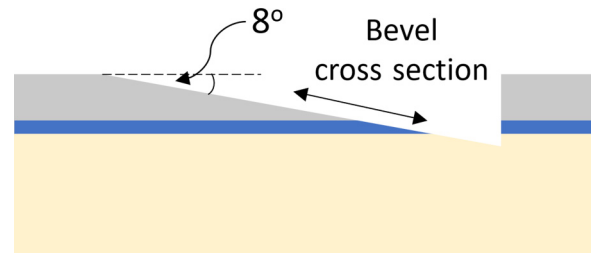

FIG. 1. Schematic side-on view of a focused ion-beam milled bevel cross section. Due to the shallow 8° bevel angle, blue and gray thin-film layers appear elongated in cross section. Diagram not drawn to scale.

to 200 nm causes a redshift in long wavelength photons generating a photocurrent. The redshift is caused by Se inter-diffusion and band gap narrowing in CST alloys with Se concentrations below $x \sim 0.4$ [5]. Previous investigations [25] on CdS-CdTe devices showed that S inter-diffusion primarily occurred during CSS deposition of CdTe, with chlorine activation producing little change in the diffusion profile due to its lower temperature. Since the thermal history of our CdSe-CdTe devices is similar, we expect the majority of Se inter-diffusion to take place during absorber layer deposition. For the 400 nm CdSe device, there is a dramatic decrease in photocurrent collection across the majority of wavelengths, despite the smaller band gap. A similar EQE trend was reported in Refs. [6,7,26] and has been attributed to the formation of a photoinactive wurtzite CST phase above $x = 0.6$ Se concentration [7], although a recent study [26] has disputed this. The EBSD and TEM results presented below, however, unambiguously confirm that there is no wurtzite phase in our devices. Other mechanisms must therefore cause the large decrease in EQE observed at 400 nm CdSe layer thickness.

Figure 2(b) shows the current density-voltage curves for the highest efficiency devices at a given CdSe layer thickness, i.e., the same devices for which the EQE is plotted in Fig. 2(a). Figures 2(c)–2(f) are box plots of the short circuit current density (J_{SC}), open circuit voltage (V_{OC}), fill factor (FF), and efficiency measured for the different devices. Numerical values for the device parameters are given in the Supplemental Material [27]. The 400 nm CdSe device has a comparatively poor J_{SC}, consistent with Fig. 2(a). Band gap narrowing in CdSe$_x$Te$_{1-x}$ will decrease the maximum attainable V_{OC}, although no clear trend is observed in Fig. 2(d). Besides the band gap, there are many other factors that can influence V_{OC}. For example, Se alloying can increase the carrier lifetime [8–10], as well as modify interfacial band alignments in the chemically graded absorber layer [28]. Series and shunt resistances can also have an effect, such as the "roll over" due to the back contact barrier [29], observed in the 50 and 100 nm CdSe
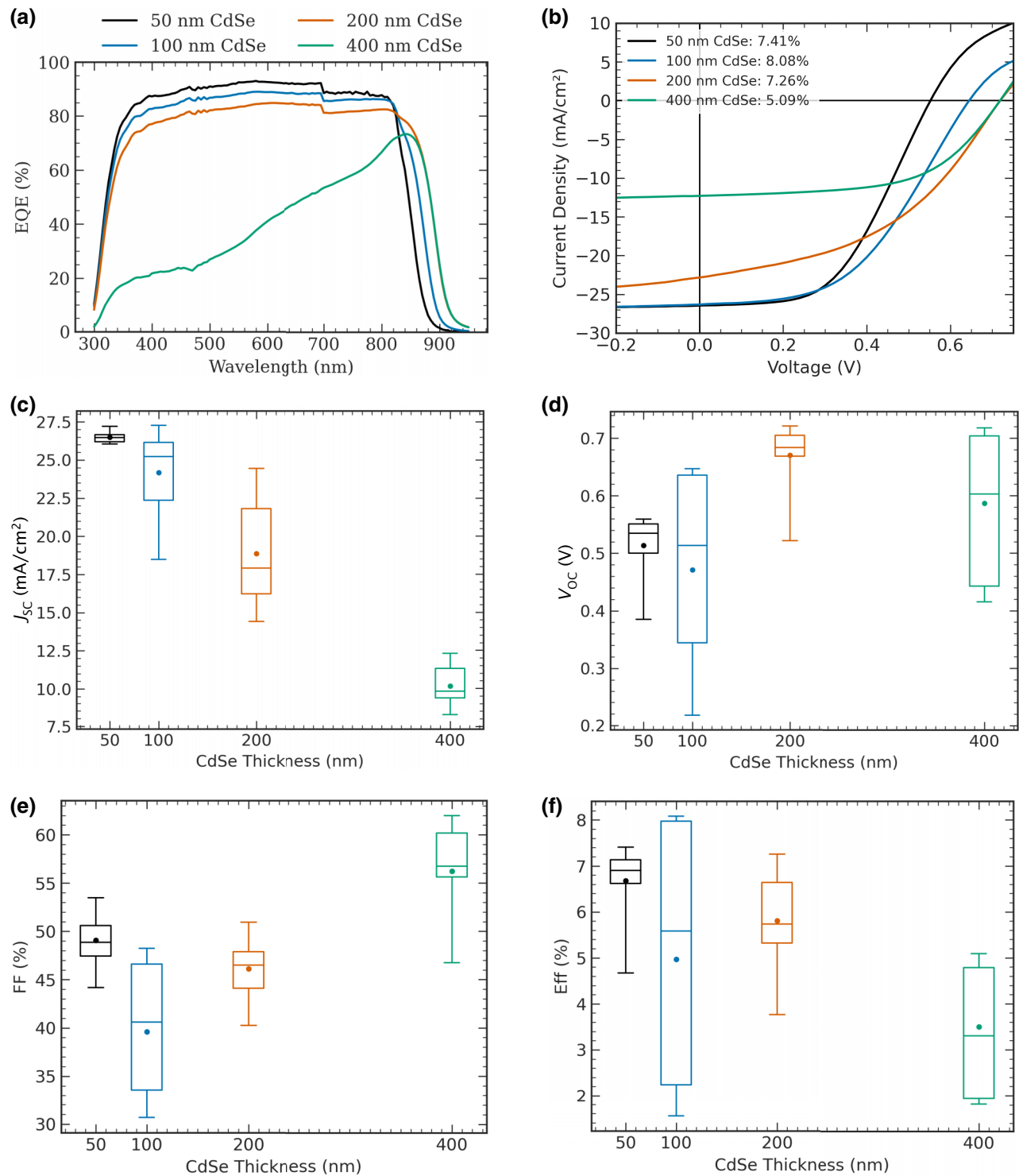
FIG. 2.   (a) External quantum efficiency for devices with variable CdSe layer thickness (50, 100, 200, and 400 nm). Results are shown for the device with highest efficiency measured at a given CdSe layer thickness. Corresponding current density-voltage graphs are shown in (b). Short circuit current density (J_{SC}), open circuit voltage (V_{OC}), fill factor (FF), and efficiency for all devices are plotted in (c)–(f).

devices shown in Fig. 2(b). The focus of this work is, however, the dramatic decrease in EQE and J_{SC} observed for thicker CdSe layers. In the following sections, we

investigate the reasons for these changes by performing an in-depth microstructural characterization of the 100 and 400 nm CdSe devices. The former has a near optimum

photocurrent collection [Fig. 2(a)], so that comparing the two microstructures should provide valuable insights into the underlying mechanism(s).

A. 100 nm CdSe device microstructure

Figures 3(a) and 3(b) show simultaneously acquired SEM secondary electron and panchromatic CL images of the 100 nm CdSe device bevel cross section (the latter maps the total luminescence signal at each electron beam

scan position). The former shows a thin porosity region in the absorber layer, with a width of about 300 nm after correcting for image distortion due to the bevel angle. Non-radiative recombination at the grain boundaries decreases the local luminescence signal, providing sufficient contrast to visualize the grain structure of the absorber layer in the panchromatic CL image. Care must be taken when interpreting the microstructure of bevel cross sections; since the bevel angle is only 8°, the observed grain size is approximately the grain diameter at a particular depth
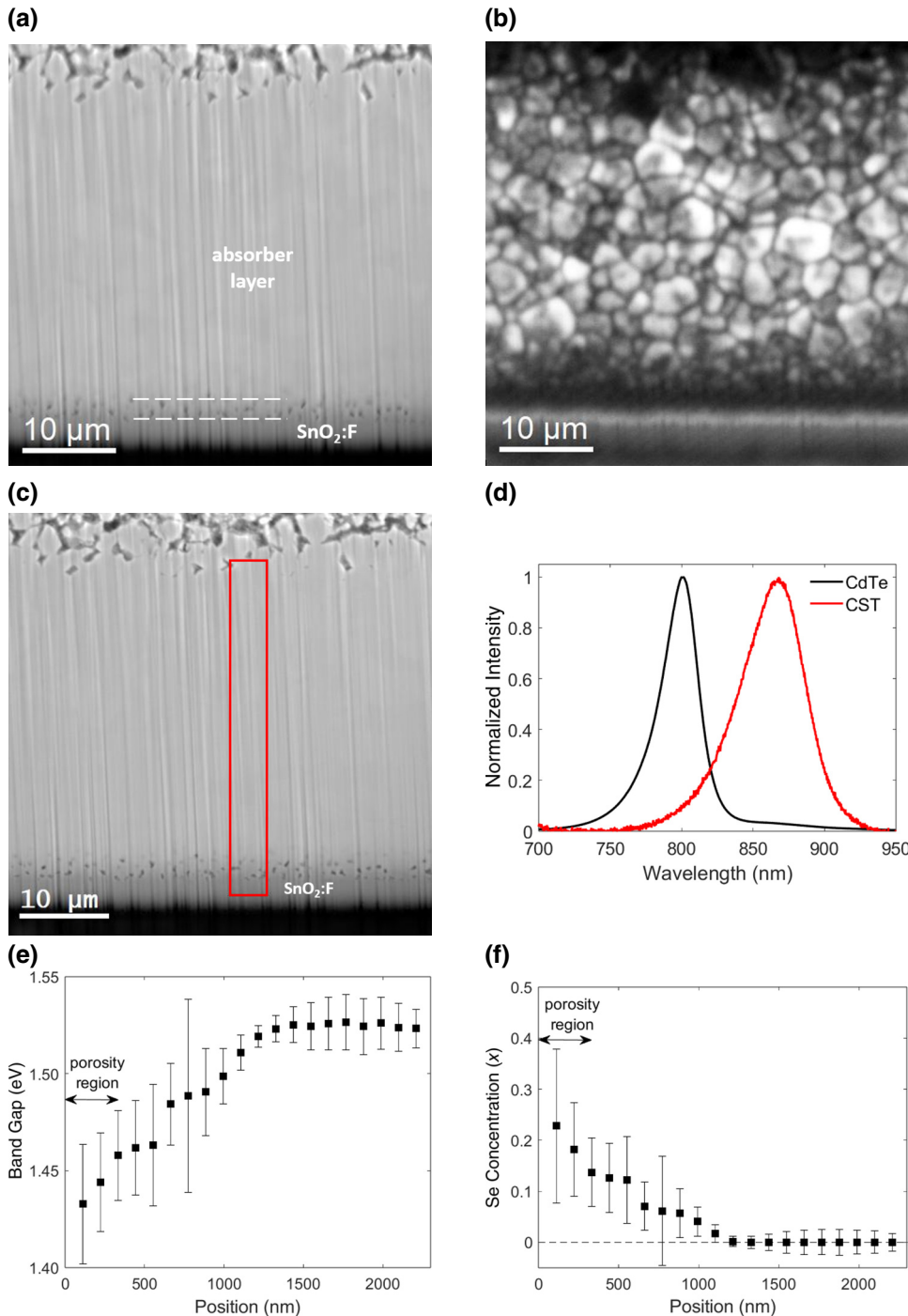

FIG. 3. Simultaneously acquired secondary electron (a) and panchromatic CL (b) images for the 100 nm CdSe bevel cross section. Horizontal dashed lines in (a) indicate the boundaries of the porosity region (SnO_2:F is the transparent conducting oxide). (c) Secondary electron image with the region of hyperspectral CL mapping indicated with a red box. CL spectra extracted from the porosity region (labeled "CST") and from close to the absorber layer back surface (labeled "CdTe") are superimposed in (d). Maximum intensity of each spectrum is normalized for a direct visual comparison. (e) Band gap grading and (f) Se concentration profiles extracted from the hyperspectral map.

within the absorber layer. From Fig. 3(b), the grains are of approximately uniform size and equiaxed throughout the absorber layer. Furthermore, the panchromatic CL image is slightly darker in the porosity region, which is likely due to higher levels of nonradiative recombination occurring at the free surfaces associated with void formation. Note that for a bevel geometry there will also be a reduction in the CL intensity close to the SnO_2:F interface due to a thinner absorber layer along the electron beam direction (Fig. 1). However, we believe this to be a secondary effect, due to the close spatial overlap between the dark panchromatic CL contrast and porosity layer. In fact, the same trends are observed for the 400 nm CdSe sample, where the porosity layer is significantly wider (Sec. III B), which suggests that a bevel geometry is not the primary contributing factor.

Spatially resolved CL spectra were examined by acquiring a hyperspectral map across the thickness of the absorber layer [Fig. 3(c)]. Average CL spectra measured from within the porosity region and towards the absorber layer back surface are shown superimposed in Fig. 3(d) (labeled "CST" and "CdTe" for reasons that will become clear later). Both spectra are asymmetrical in shape, with a longer "tail" on the short wavelength (high photon energy) side, and furthermore, the spectrum from the porosity region is broader and redshifted compared to the absorber layer back surface. The detection of CL intensity above the CdTe band gap (816 nm wavelength) indicates that these spectra represent near band edge luminescence, where a conduction band electron radiatively recombines with a valence band hole [30,31]. The peak emission in the near band edge luminescence is at about $E_g + kT/2$, where E_g is the band gap, k is the Boltzmann constant, and T is temperature. The CL spectrum at the absorber layer back surface can therefore be attributed to CdTe, while the lower peak energy for the porosity region signifies a lower band gap, most likely due to Se alloying [16]. The CdTe spectrum also shows a weak shoulder at about 873 nm, which is in a similar wavelength range to donor-acceptor pair (DAP) transitions [32]. The DAP peak is prominent at cryogenic temperatures (liquid nitrogen or helium) [33] but is much weaker in Fig. 3(d) due to partial ionization of the defect levels at room temperature [31], the temperature at which the CL data were acquired. The near band edge intensity, $I(E)$, can be approximated by [34]

$$I(E) = A\sqrt{E - E_g}\exp\left[-\frac{(E - E_g)}{kT}\right], \quad (1)$$

where A is a proportionality constant and E is the photon energy. The square root term is due to the optical joint density of states, while the exponential is derived from the Fermi-Dirac distribution of carriers at a given temperature [34]. Note that a more precise expression for near band edge intensity can be derived using the principle of detailed balance [31], although we have found that the

(simpler) Eq. (1) is also a good fit to the experimental data. Equation (1) predicts that the near band edge luminescence profile only depends on the energy difference $(E - E_g)$. The broadening of the redshifted CL spectrum for the porosity region [Fig. 3(d)] is therefore largely due to the inverse relationship between photon energy and wavelength; other contributing factors to broadening could be spatial inhomogeneities in the alloy composition.

A plot of $[I(E)e^{E/kT}]^2$ against E is a straight line, with E_g being equal to the negative ratio of the intercept divided by the gradient. This method was applied to the hyperspectral CL data in Fig. 3(c) to determine the local band gap as a function of position within the absorber layer. Hyperspectral map pixels were horizontally binned to generate a 1D line profile, so that the local band gap at a given position is the average of several grains. Furthermore, the luminescence profile to the left of the peak intensity [i.e., shorter wavelengths in Fig. 3(d)] was used for extracting E_g, with the necessary corrections [34] made when converting $I(\lambda)$ into $I(E)$, where λ is the photon wavelength. The extracted band gap grading is shown in Fig. 3(e). The regression coefficient for the straight line fit was above 0.9 for all data points, indicating that the luminescence profile was satisfactorily represented by Eq. (1). Moving towards the front interface, the band gap decreases from the CdTe value (1.52 eV) to 1.43 eV in the porosity region, with the full width of the transition extending over a distance of about 1300 nm. The change in band gap is due to Se alloying.

The Se concentration (x) in CdSe$_x$Te$_{1-x}$ can be calculated from the local band gap, E_g, using the following quadratic equation in x [5]:

$$E_g = xE_g(\text{CdSe}) + (1 - x)E_g(\text{CdTe}) - bx(1 - x), \quad (2)$$

where $E_g(\text{CdSe}) = 1.74$ eV and $E_g(\text{CdTe}) = 1.52$ eV are the CdSe and CdTe band gaps, respectively, and $b = 0.78$ eV is the bowing parameter [5]. Applying Eq. (2) to Fig. 3(e) gives the Se diffusion profile shown in Fig. 3(f). Some of the data points close to the absorber layer back surface had band gap values slightly above that of pure CdTe, due to the error in the measurement. These values were "rounded" to 1.52 eV to avoid nonphysical solutions to the composition. The maximum Se concentration, $x = 0.2$, is found in the porosity region and is well below the CdSe composition, $x = 1.0$. This suggests that the CdSe layer has been fully dissolved by inter-diffusion.

TEM was used for high spatial resolution crystal structure and chemical analysis. Figures 4(a) and 4(b) show STEM bright field and dark field images of the 100 nm CdSe device cross section. A thin ($\sim$200–400 nm) porosity layer [see arrows in Fig. 4(b)] is observed at the interface between the SnO_2:F transparent conducting oxide and absorber layer, consistent with the SEM result [Fig. 3(a)].
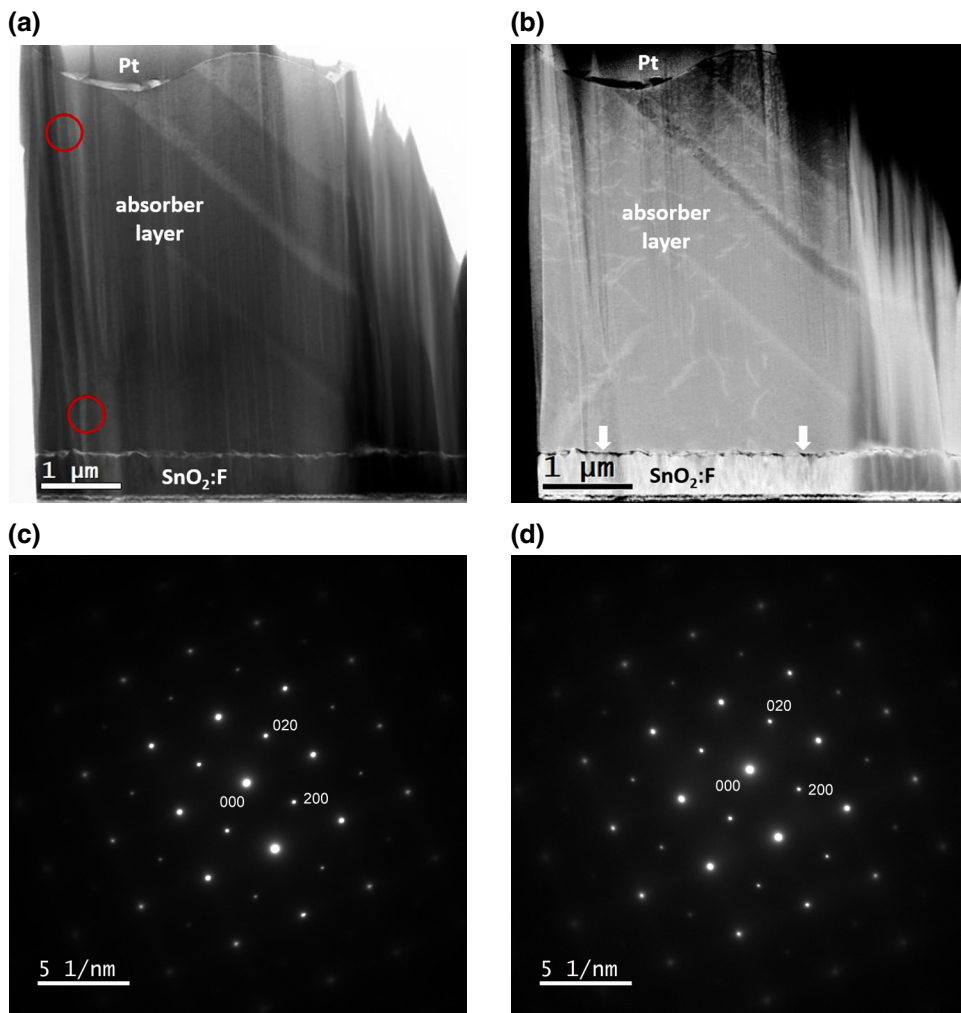
(a)

(b)

FIG. 4. STEM bright field (a) and dark field (b) images of the 100 nm CdSe device. Pt is a protective layer used during FIB TEM specimen preparation, while SnO_2:F is the transparent conducting oxide. Note that part of the TEM cross section has been damaged by FIB milling during specimen preparation. Arrows in (b) indicate porosity in the absorber layer. Selected area electron diffraction patterns acquired from the top and bottom red circle regions in (a) are shown in (c),(d), respectively.

(c)

(d)

The absorber layer in the field of view consists of a columnar grain extending through the entire layer thickness. This is confirmed by tilting the grain to a zone axis and acquiring selected area diffraction patterns from the top and bottom regions of the absorber layer at the same specimen tilt. The two diffraction patterns [Figs. 4(c) and 4(d)] are nearly identical and can be indexed as the [001] zone axis of the cubic zinc blende crystal structure. Note that Se inter-diffusion will slightly change the unit cell dimensions [5], but for cubic crystals the diffraction patterns can still be indexed independently of the lattice parameter by taking ratios of inter-planar spacings [35]. EBSD phase mapping of the bevel cross section (Fig. 5) also indicates that the grains have cubic zinc blende crystal structure throughout the absorber layer (here, zinc blende CdTe and wurtzite CdSe crystal structures were used as references for phase identification). Finally, the results from STEM EDX chemical mapping of the columnar grain in Fig. 4(a) are shown in Fig. 6. The presence of Se directly confirms that the band gap grading observed in Fig. 3(e) is due to inter-diffusion, and not due to other factors, such as a change in crystal

structure. There is also no evidence of a separate CdSe layer, indicating its complete dissolution.

The integrated 1D line profile for the Se EDX map indicated a diffusion distance for the columnar grain in excess of 2000 nm, considerably larger than the average CL result in Fig. 3(f) (see the Supplemental Material [27]). The discrepancy is because the STEM EDX measurement is for a single absorber layer grain, while the CL hyperspectral mapping area includes multiple grains from different regions of the sample in the bevel cross section (Fig. 1). The latter is therefore an average, and hence more representative, measurement of Se diffusion. The electron beam-specimen interaction volume could also potentially affect the CL measurement. Estimating the size of the interaction volume is difficult, due to nonuniform generation of electron-hole pairs and carrier diffusion within the material. Nevertheless, even an interaction volume as large as 1000 nm in diameter corresponds to an absorber layer distance of only about 140 nm, after correcting for the 8° bevel angle. This is significantly smaller than the Se diffusion distance of about 1300 nm measured by
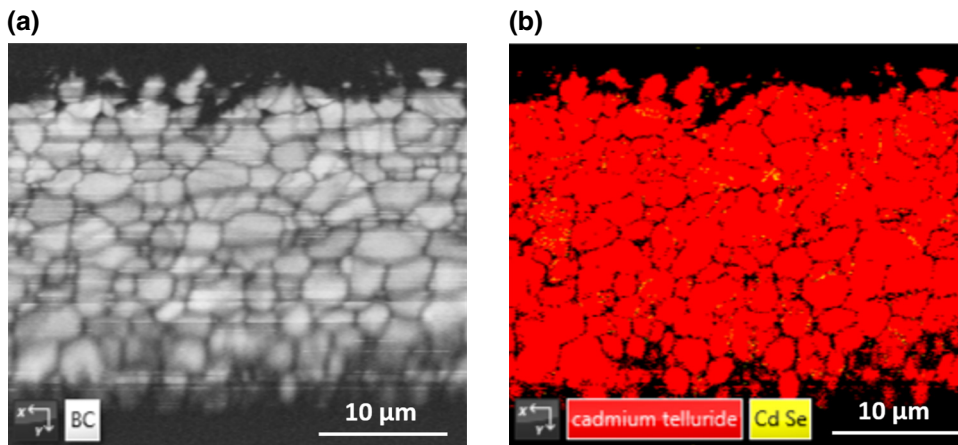
(a)

(b)

FIG. 5. EBSD pattern quality (a) and phase map (b) for the 100 nm CdSe absorber layer (bevel cross section). EBSD patterns were matched against cubic zinc blende CdTe (red) and hexagonal wurtzite CdSe (yellow) reference phases. All grains in the absorber layer are identified as being cubic.

hyperspectral CL mapping, indicating that beam interaction volume artefacts can be largely ignored for our specimens.

B. 400 nm CdSe device microstructure

CL, TEM, and EBSD characterization was also performed on the 400 nm CdSe device. Figures 7(a) and 7(b) are simultaneously acquired SEM secondary electron and panchromatic CL images of the bevel cross section. Compared to the 100 nm CdSe device, there is a much larger porosity region evident in the secondary electron image. The width of the porosity region is 2140 nm (after correcting for image distortion) and appears dark in the panchromatic CL image. Close examination of Fig. 7(b) shows that the grain size is much smaller in the porosity region, and many of the pores form at the grain boundary triple points (further evidence corroborating these claims is presented below). The reduced CL intensity is due to increased nonradiative recombination from the grain boundaries and voids. The larger area of nonradiative recombination overlaps with the space charge region, where much of the photocurrent is generated [36]. The inevitable loss in photogenerated carriers is likely to be the origin of the reduced EQE for this device.

CL hyperspectral mapping [Fig. 7(c)] is performed to determine the band gap grading [Fig. 7(d)] and Se concentration profile [Fig. 7(e)], using the procedure described in the previous section. There is no evidence of a 1.74 eV CdSe band gap, indicating that the 400 nm CdSe layer has fully dissolved, despite its larger thickness. The diffusion zone is at least 2600 nm wide [the lower limit is because the hyperspectral map in Fig. 7(c) does not span the full porosity region]. The band gap converges to about 1.41 eV deep within the porosity region [Fig. 7(d)]. This is slightly below the minimum band gap (1.42 eV) predicted by Eq. (2), and therefore, a Se concentration cannot be calculated for these data points [Fig. 7(e)], although we expect a value close to the band gap minimum composition

of $x \sim 0.4$. Furthermore, some of the data points near the absorber layer back surface had a band gap slightly larger than 1.52 eV; these were assigned as being pure CdTe.

The STEM bright field [Fig. 8(a)] and dark field [Fig. 8(b)] images show smaller equiaxed absorber layer grains at the interface with the SnO_2:F layer. The typical interfacial grain diameter is several hundred nanometers [the EBSD pattern quality map in Fig. 9(a) gave an average grain diameter of (783 ± 245) nm]. Porosity is also evident at the SnO_2:F interface, as well as some of the grain boundary triple points [see arrows in Fig. 8(b)]. The crystal structure of one such small interfacial grain [Fig. 8(c)] was determined by selected area electron diffraction. The zone-axis diffraction pattern in Fig. 8(d) was indexed as $[1\bar{1}\bar{1}]$ cubic zinc blende. To unambiguously confirm the crystal structure, the same grain was tilted by 19.9° to a new zone axis [Fig. 8(e)], which was indexed as being along the cubic $[11\bar{2}]$ direction, consistent with both the symmetry of the diffraction pattern and specimen tilt angle. Further confirmation of a cubic zinc blende crystal structure is obtained via EBSD phase mapping (Fig. 9). Some of the small grains, however, are not identified due to a poor EBSD pattern quality. It is believed that this is due to specimen preparation artefacts from FIB polishing, specifically curtaining striations [24] around individual pores (see Supplemental Material [27]). Neither TEM nor EBSD, therefore, provide evidence of a hexagonal wurtzite CST phase, which has previously been reported to degrade the EQE [7]. STEM EDX mapping results for the 400 nm device are shown in Fig. 10. The small interfacial grains are rich in Se, but inter-diffusion extends further, and as far as 1200 nm into the absorber layer (see the Supplemental Material [27]), a smaller value than the average diffusion distance measured by CL [Fig. 2(e)]. There is also no evidence of a CdSe layer, indicating that it has fully dissolved during inter-diffusion.

It was previously reported that Se diffused faster along the grain boundaries [11,16]. To confirm if this was also
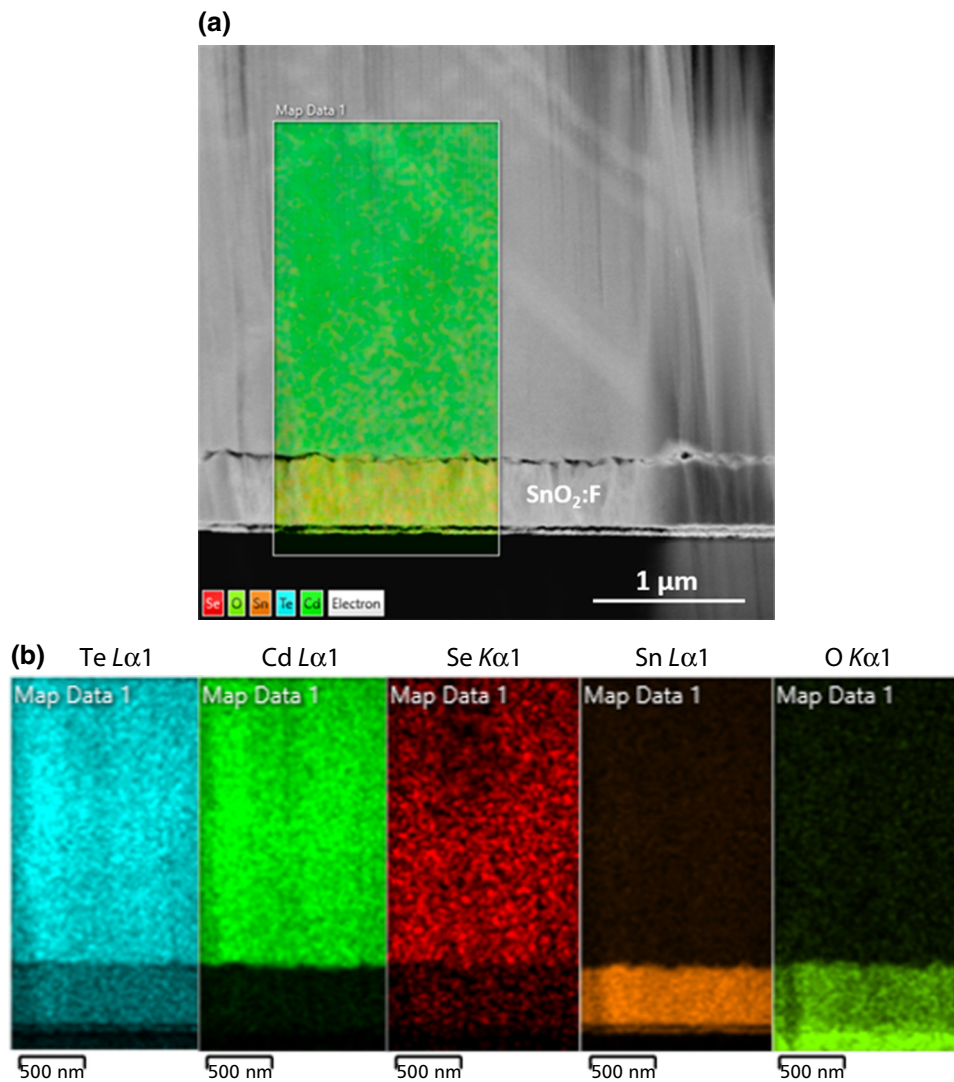
(a)

FIG. 6. (a) STEM dark field image of the 100 nm CdSe device with EDX false color image superimposed over the map region. Te $L\alpha$, Cd $L\alpha$, Se $K\alpha$, Sn $L\alpha$, and O $K\alpha$ EDX x-ray maps are shown in (b). Presence of Te in the SnO_2:F layer is an artefact due to energy overlap between Te $L\alpha$ and Sn $L\alpha$ x-ray peaks. Scale bar for each of the EDX maps is 500 nm.

true of our devices, we performed hyperspectral CL mapping of the transition region between the small interfacial grains and larger grains found in the rest of the absorber layer [Fig. 11(a)]. This region still has some amount of Se inter-diffusion, which should occur predominantly along the grain boundaries, provided they are fast diffusion pathways. The smaller grain boundary curvature for larger grains also makes it easier to detect any Se at the grain boundaries using CL. Gaussian functions were least-squares fitted to the near band edge luminescence peak at each pixel in the hyperspectral map. The amplitude and peak wavelength of the fitted Gaussians are mapped in Figs. 11(b) and 11(c), respectively. The latter shows a clear redshift at the grain boundaries, indicating a higher local Se concentration. Example CL spectra from a grain interior and neighboring grain boundary are displayed in Fig. 11(d). The wavelength redshift in this case is about 6 nm. It is concluded that Se preferentially diffuses along the grain boundaries in our samples as well.

C. Absorber layer grain growth mechanism

It is clear that grain morphology can have an important effect on photocurrent collection in CdSe-CdTe devices. Large amounts of Se inter-diffusion from thicker CdSe layers result in small grain sizes, as well as grain boundary porosity, which collectively increase nonradiative recombination. Changes in grain structure during chlorine activation were observed previously in CdTe thin-film photovoltaics and attributed to recrystallization [37,38] and grain growth phenomena [39]. However, there is good reason to believe that such processes do not occur in our devices. First, any Se diffusion will lower the local lattice mismatch, thus suppressing the driving forces (i.e., strain energy) for recrystallization. Second, recrystallization is not known to induce grain boundary porosity, which is observed in our samples. Third, the high temperature deposition conditions in close space sublimation generally favor the formation of large grains, which remain unaltered during subsequent (lower temperature)
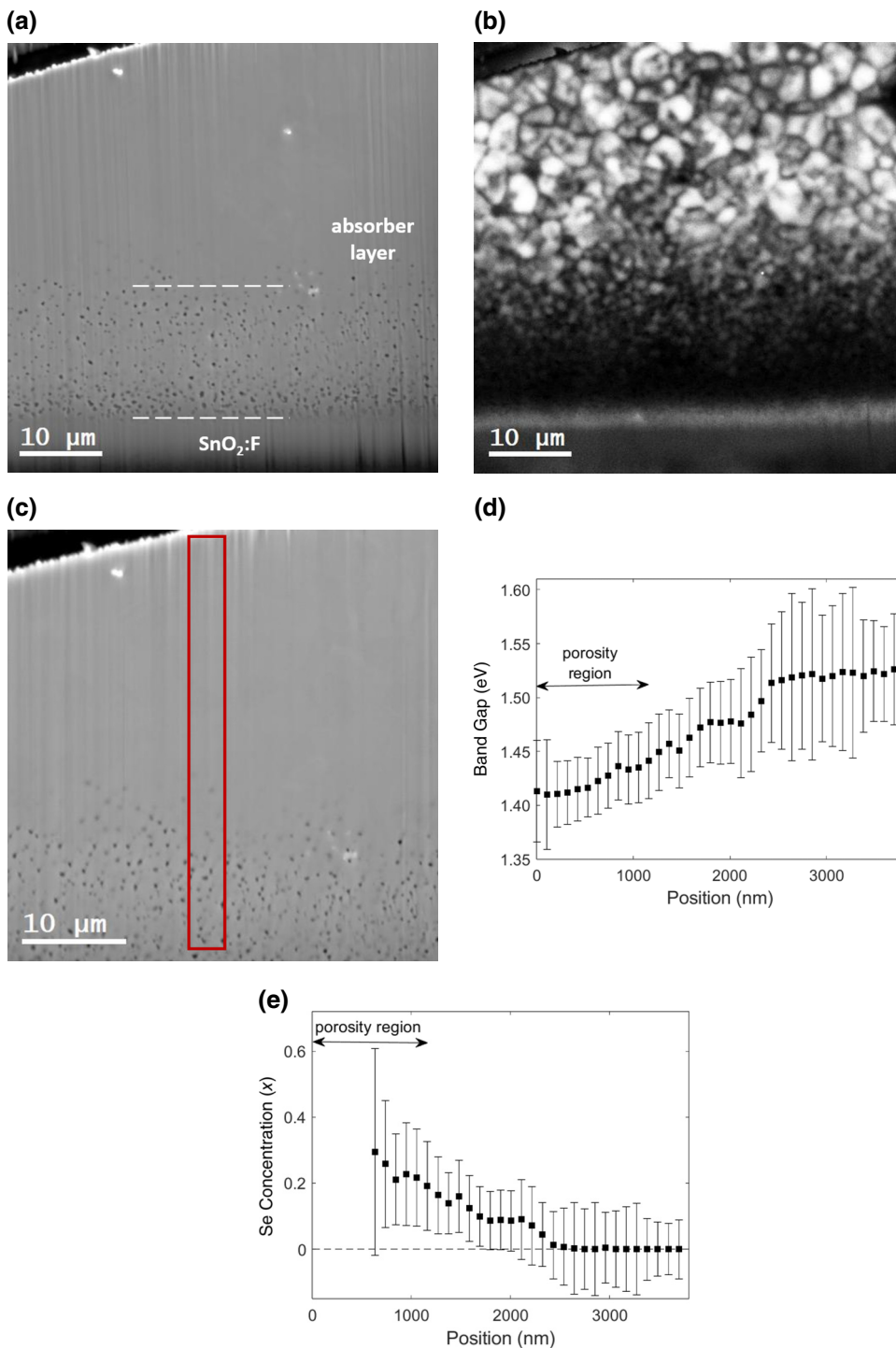
FIG. 7. Simultaneously acquired secondary electron (a) and panchromatic CL (b) images for the 400 nm CdSe bevel cross section. Horizontal dashed lines in (a) indicate the boundaries of the porosity region (SnO_2:F is the transparent conducting oxide). (c) Secondary electron image with the region of hyperspectral CL mapping indicated with a red box. (d) Band gap grading and (e) Se concentration profiles extracted from the hyperspectral map. Some of the data points within the porosity region in (e) are not shown due to complications in calculating the Se concentration; see text for further details.

device processing steps, such as chlorine activation [38]. Indeed, the grain size distribution in our CSS-grown CdSe-CdTe films has been shown to be very stable to postgrowth processing [21,25]. A more straightforward explanation for the small grain size and grain boundary porosity instead lies in the faster diffusion of Se along grain boundaries and free surfaces. The salient features of our proposed model are illustrated in Fig. 12.

In the early stages (Fig. 12, left panel) CSS-deposited CdTe exhibits island growth [40], due to the large (14%) lattice mismatch with the underlying CdSe layer. Data in Ref. [16] suggest that, at the substrate deposition temperature of 550 °C (Sec. II), the Se diffusion coefficient along grain boundaries is 3 orders of magnitude larger than bulk lattice diffusion. It is reasonable to assume a similarly large enhancement for surface diffusion as well. The surface of the CdTe island nuclei will therefore be decorated with

(a)
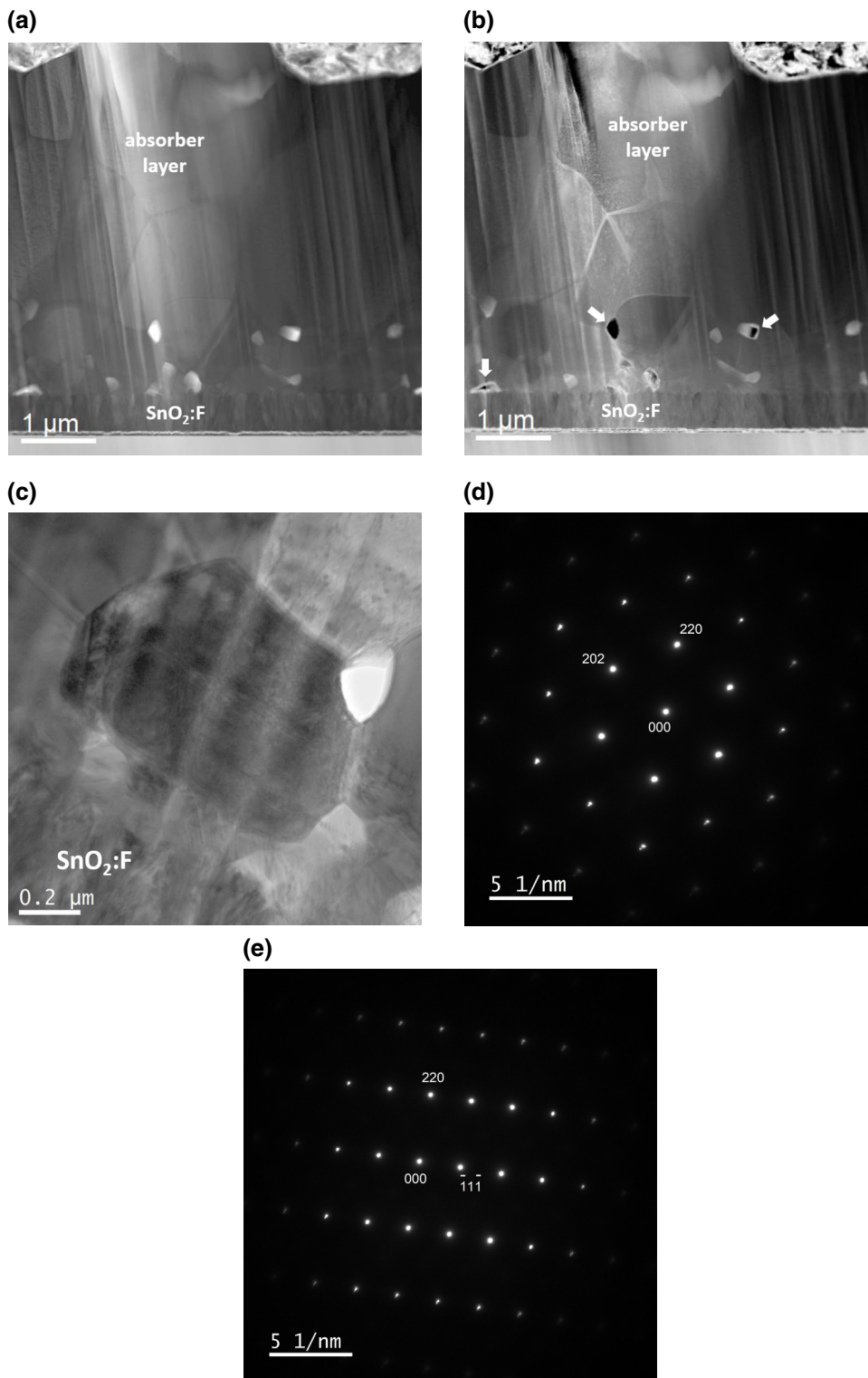
(b)

(c)

(d)

(e)

FIG. 8. STEM bright field (a) and dark field (b) images of the 400 nm CdSe device. Arrows in (b) indicate porosity in the absorber layer. (c) Many-beam bright field TEM image of an absorber layer grain (image center) close to the SnO$_2$:F interface. Two selected area electron diffraction patterns acquired from this grain at different specimen tilts are shown in (d),(e).

Se atoms, while a few Se atoms may also diffuse into the islands through the much slower process of lattice diffusion. As CSS deposition proceeds, more Cd and Te atoms will arrive from the vapor phase and potentially form adatoms on bare CdSe, which can then diffuse towards the CdTe islands. The resulting island growth "traps" the existing Se surface atoms to form a Se-rich outer layer (Fig. 12, center panel). In this manner, the Se concentration within the islands is increased, although the composition is nonuniform. The surfaces of the islands remain decorated with Se, due to fast surface diffusion. Grain boundaries are formed when neighboring islands impinge on one another.
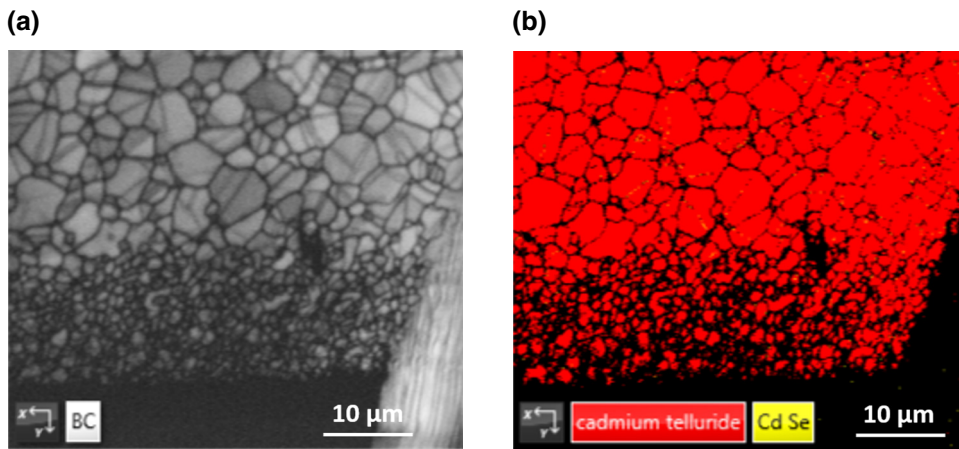
(a)

(b)

FIG. 9. EBSD pattern quality (a) and phase map (b) for the 400 nm CdSe absorber layer (bevel cross section). EBSD patterns were matched against cubic zinc blende CdTe (red) and hexagonal wurtzite CdSe (yellow) reference phases. All indexed grains in the absorber layer are cubic, although for some small grains at the bottom it was not possible to identify the phase due to poor pattern quality.

The merging of two Se-rich surfaces results in a grain boundary with a high local Se concentration (Fig. 12, right panel). Lattice diffusion would also tend to homogenize the Se composition within the island interiors. After the islands have merged, further Se inter-diffusion from the remaining CdSe layer predominantly occurs along the grain boundaries.

DFT calculations [13,14] indicate that Se has a lower energy at a CdTe grain boundary compared to the grain interior, so segregation of Se to the grain boundaries is expected. During grain growth, the moving grain boundary must ideally preserve the equilibrium segregation profile for energetic reasons. However, if Se atom diffusion is slow with respect to the grain boundary velocity, the
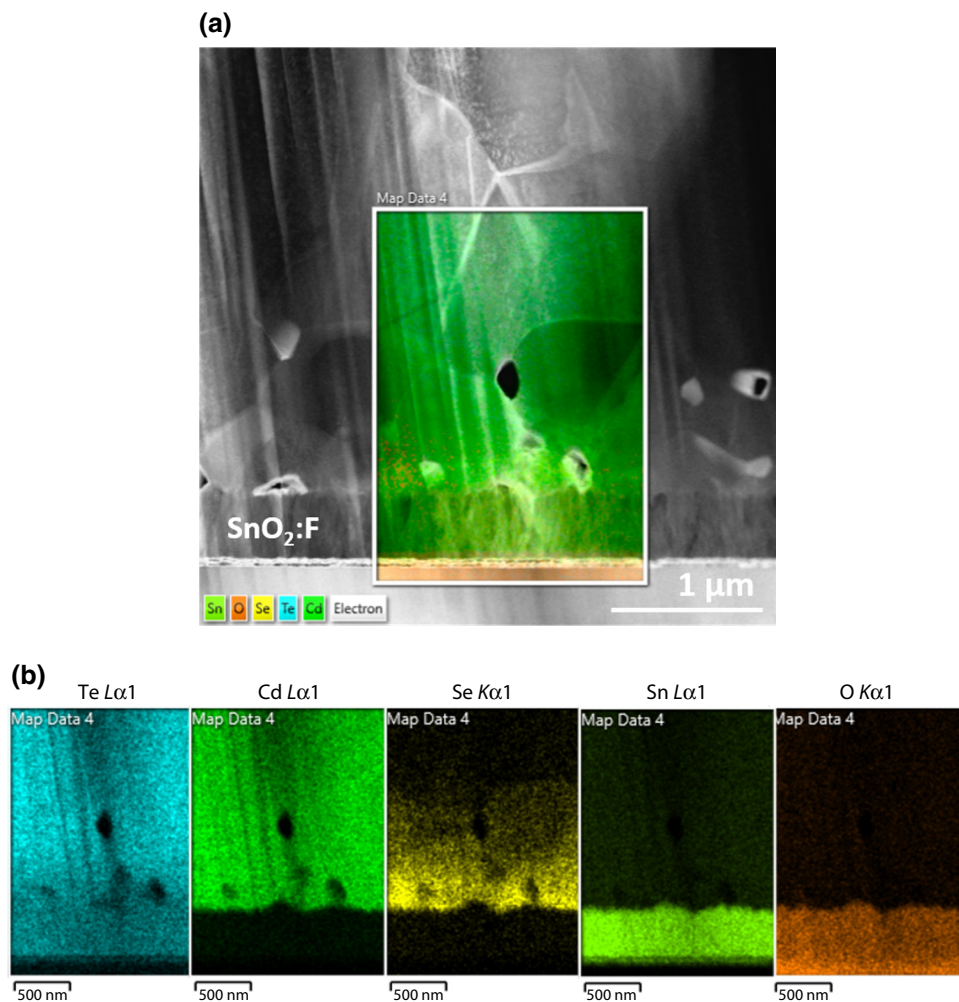
(a)

FIG. 10. (a) STEM dark field image of the 400 nm CdSe device with EDX false color image superimposed over the map region. Te $L\alpha$, Cd $L\alpha$, Se $K\alpha$, Sn $L\alpha$, and O $K\alpha$ EDX x-ray maps are shown in (b). Presence of Te in the SnO$_2$:F layer is an artefact due to energy overlap between Te $L\alpha$ and Sn $L\alpha$ x-ray peaks. Scale bar for each of the EDX maps is 500 nm.

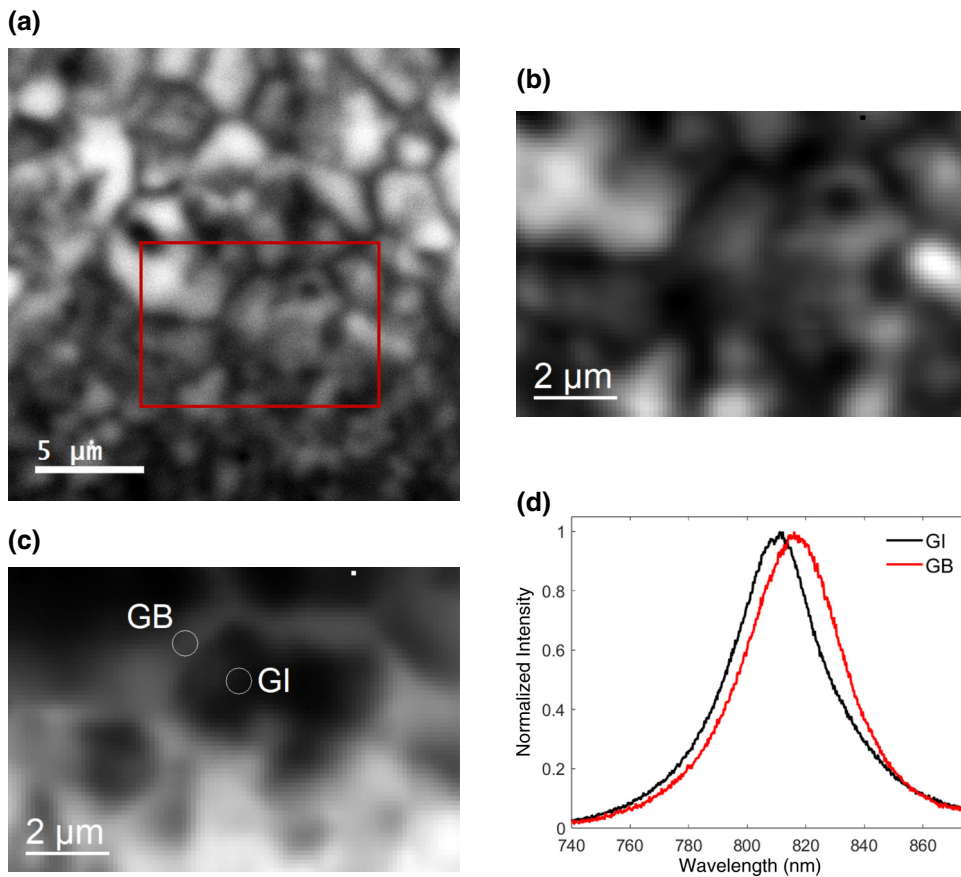**(b)**

(a)

(b)

(c)

(d)

FIG. 11. (a) Panchromatic CL image of the transition region between the small interfacial grains (image bottom) and the rest of the absorber layer in the 400 nm CdSe sample. Red box denotes the area used for hyperspectral CL mapping. Gaussian functions were fitted to each pixel in the hyperspectral map. In (b), the amplitude of the Gaussian is mapped, where white represents 683 counts and black 97 counts. (c) Peak wavelength of the fitted Gaussian, where white and black correspond to 842 and 808 nm, respectively. Images appear pixelated due to fewer electron beam scan positions being used in hyperspectral mapping. (d) CL spectra extracted from a grain boundary and neighboring grain interior labeled "GB" and "GI," respectively, in (c). Peak intensity for each spectrum has been normalized for direct visual comparison.

steady-state concentration profile will deviate from equilibrium. The energy increase of the nonequilibrium profile exerts a drag force on the moving grain boundary [17]. The CST grain size will therefore be smaller compared to pure CdTe. The presence of voids at the grain boundaries can be explained by the grain boundary Kirkendall effect [19,41]. In substitutional alloys, a net vacancy flux is produced if the diffusion rates of the constituent atoms are not equal. In the present example, Se diffuses faster into CdTe compared to Te diffusion into CdSe. The vacancy flux is accommodated by climbing of edge dislocations, with any excess vacancies forming voids [19]. Porosity is mainly observed at the grain boundaries where Se diffusion is fastest, with the grain boundary triple points appearing to be particularly favorable nucleation sites for the voids. Grain boundary porosity may further inhibit grain growth through the Zener pinning mechanism [42]. Previous investigations have revealed lower CL contrast at CST grain boundaries compared to CdTe [10,12], which suggests that Se has a passivating role. Nevertheless, CST grain boundaries still appear darker in CL compared to the grain interior, indicating that some residual nonradiative
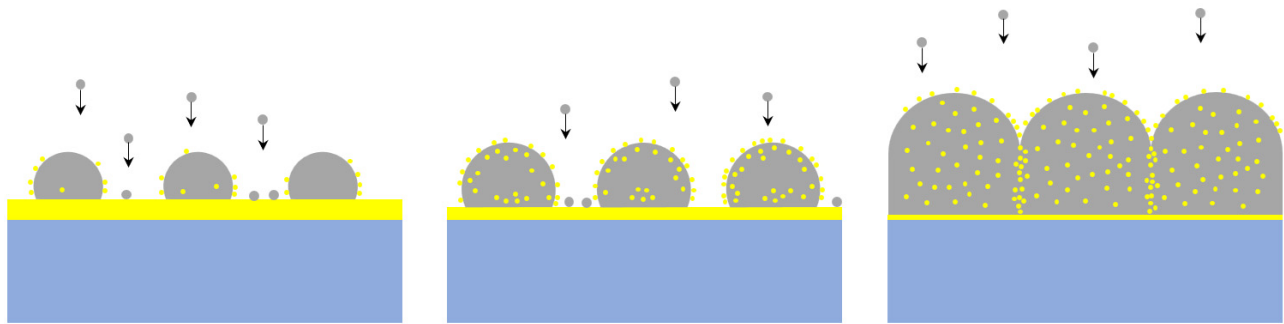

FIG. 12. Schematic illustration of the proposed grain growth mechanism in CdSe-CdTe photovoltaics during close space sublimation. Cd and Te atoms in the vapor phase and as adatoms are denoted in gray. They form CdTe islands, which eventually merge into grains (also colored gray). CdSe layer and Se atoms are denoted in yellow. Underlying substrate is blue. See text for further details.

recombination is still present at the grain boundary, despite passivation. Therefore, if solute drag produces sufficiently small grains, the net effect of the larger grain boundary area, together with grain boundary voids, would be an increase in nonradiative recombination.

Our investigations have been on CdSe-CdTe devices, and it is interesting to speculate if the above has any bearing on co-deposited devices. Islands of co-deposited CST are naturally alloyed with Se, and there is no inter-diffusion from an underlying Se reservoir. When the islands merge, Se must diffuse through the lattice to establish the equilibrium Se segregation profile at the grain boundary. This is a slower process compared to grain boundary or surface diffusion, so a smaller drag force is expected during grain growth. In Ref. [9], micrographs of the co-deposited CST layer do indeed show a smaller grain size compared to the overlying CdTe layer (see Fig. 6 in Ref. [9]). Furthermore, in Ref. [11], there is clear evidence of grain boundary porosity at the interface between CST and CdTe layers, where inter-diffusion occurs (see Fig. 1 in Ref. [11]). However, in all these cases, the solute drag and grain boundary porosity was not sufficiently strong to produce high levels of nonradiative recombination, and the CST layer appeared brighter in the CL image compared to CdTe, due to the passivating role of Se within the grain interiors.

IV. SUMMARY

The microstructural causes for the decrease in photocurrent collection in CdSe-CdTe devices with thick CdSe layers was investigated using electron microscopy. Previous reports have attributed the lower EQE to formation of a photoinactive hexagonal wurtzite CST phase at high Se concentration. TEM and EBSD analysis, however, confirmed that the absorber layer crystal structure in our devices remained cubic zinc blende, suggesting other mechanisms were responsible for the lower device performance. Smaller grain sizes of about 783 nm and grain boundary porosity were observed at the Se interdiffusion zone. The decrease in CL intensity within this region suggests higher levels of nonradiative recombination, which would lead to a lower photocurrent. Furthermore, evidence for faster Se diffusion along grain boundaries was also observed, consistent with previous results in the literature. Grain boundary solute drag and Kirkendall voiding are proposed as plausible mechanisms that can explain the microstructural changes occurring during Se inter-diffusion. When the material processing is not optimized, these physical changes can act to severely limit the performance of CdSe-CdTe photovoltaics.

ACKNOWLEDGMENTS

[1] M. A. Green, E. D. Dunlop, M. Yoshita, N. Kopidakis, K. Bothe, G. Siefer, and X. Hao, Solar cell efficiency tables (version 63), Prog. Photovoltaics **31**, 651 (2023).

[2] D. E. Swanson, J. R. Sites, and W. S. Sampath, Co-sublimation of $CdSe_xTe_{(1-x)}$ layers for CdTe solar cells, Sol. Energy Mater. Sol. Cells **159**, 389 (2017).

[3] T. Baines, G. Zoppi, L. Bowen, T. P. Shalvey, S. Mariotti, K. Durose, and J. D. Major, Incorporation of CdSe layers into CdTe thin film solar cells, Sol. Energy Mater. Sol. Cells **180**, 196 (2018).

[4] T. Baines, L. Bowen, B. G. Mendis, and J. D. Major, Microscopic analysis of interdiffusion and void formation in $CdTe_{(1-x)}Se_x$ and CdTe layers, ACS Appl. Mater. Interfaces **12**, 38070 (2020).

[5] M. Lingg, A. Spescha, S. G. Haass, R. Carron, S. Buecheler, and A. N. Tiwari, Structural and electronic properties of $CdTe_{1-x}Se_x$ films and their application in solar cells, Sci. Technol. Adv. Mater. **19**, 683 (2018).

[6] N. R. Paudel and Y. Yan, Enhancing the photo-currents of CdTe thin-film solar cells in both short and long wavelength regions, Appl. Phys. Lett. **105**, 183510 (2014).

[7] J. D. Poplawsky, W. Guo, N. Paudel, A. Ng, K. More, D. Leonard, and Y. Yan, Structural and compositional dependence of the $CdTe_xSe_{1-x}$ alloy layer photoactivity in CdTe-based solar cells, Nat. Commun. **7**, 12537 (2016).

[8] X. Zheng, D. Kuciauskas, J. Moseley, E. Colegrove, D. S. Albin, H. Moutinho, J. N. Duenow, T. Ablekim, S. P. Harvey, A. Ferguson, and W. K. Metzger, Recombination and bandgap engineering in CdSeTe/CdTe solar cells, APL Mater. **7**, 071112 (2019).

[9] T. Ablekim, J. N. Duenow, C. L. Perkins, J. Moseley, X. Zheng, T. Bidaud, B. Frouin, S. Collin, M. O. Reese, M. Amarasinghe, E. Colegrove, S. Johnston, and W. K. Metzger, Exceeding 200 ns lifetimes in polycrystalline CdTe solar cells, Sol. RRL **5**, 2100173 (2021).

[10] M. Amarasinghe, D. Albin, D. Kuciauskas, J. Moseley, C. L. Perkins, and W. K. Metzger, Mechanisms for long carrier lifetime in Cd(Se)Te double heterostructures, Appl. Phys. Lett. **118**, 211102 (2021).

[11] T. A. M. Fiducia, B. G. Mendis, K. Li, C. R. M. Grovenor, A. H. Munshi, K. Barth, W. S. Sampath, L. D. Wright, A. Abbas, J. W. Bowers, and J. M. Walls, Understanding the role of selenium in defect passivation for highly efficient selenium-alloyed cadmium telluride solar cells, Nat. Energy **4**, 504 (2019).

[12] T. Fiducia, A. Howkins, A. Abbas, B. Mendis, A. Munshi, K. Bath, W. Sampath, and J. Walls, Selenium passivates grain boundaries in alloyed CdTe solar cells, Sol. Energy Mater. Sol. Cells **238**, 111595 (2022).

[13] R. Wang, M. Lan, and S.-H. Wie, Enhanced performance of Se-alloyed CdTe solar cells: The role of Se-segregation on the grain boundaries, J. Appl. Phys. **129**, 024501 (2021).

[14] J. Guo, A. Mannodi-Kanakkithodi, F. G. Sen, E. Schwenker, E. S. Barnard, A. Munshi, W. Sampath, M. K. Y. Chan, and R. F. Klie, Effect of selenium and chlorine

co-passivation in polycrystalline CdSeTe devices, Appl. Phys. Lett. **115**, 153901 (2019).

[15] C. J. Tong and K. P. McKenna, Passivating grain boundaries in polycrystalline CdTe, J. Phys. Chem. C **123**, 23882 (2019).

[16] E. Colegrove, X. Zheng, T. Ablekim, J. N. Duenow, C. L. Perkins, H. R. Mutinho, and W. K. Metzger, Se diffusion in CdTe thin films for photovoltaics, J. Phys. D: Appl. Phys. **54**, 025501 (2021).

[17] J. W. Cahn, The impurity-drag effect in grain boundary motion, Acta Metall. **10**, 789 (1962).

[18] R. K. Koju and Y. Mishin, Direct atomistic modeling of solute drag by moving grain boundaries, Acta Mater. **198**, 111 (2020).

[19] E. Rabkin, L. Klinger, T. Izyumova, and V. N. Semenov, Diffusion-induced grain boundary porosity in NiAl, Scr. Mater. **42**, 1031 (2000).

[20] J. F. Leaver, K. Durose, and J. D. Major, in *2021 48th IEEE Photovoltaic Specialists Conference (PVSC)* (Fort Lauderdale, FL, USA, 2021), pp. 1187.

[21] M. A. Cousins and K. Durose, Grain structure of CdTe in CSS-deposited CdTe/CdS solar cells, Thin Solid Films **361–362**, 253 (2000).

[22] M. D. G. Potter, D. P. Halliday, M. Cousins, and K. Durose, A study of the effects of varying cadmium chloride treatment on the luminescent properties of CdTe/CdS thin film solar cells, Thin Solid Films **361–362**, 248 (2000).

[23] M. D. G. Potter, M. Cousins, K. Durose, and D. P. Halliday, Effect of interdiffusion and impurities on thin film CdTe/CdS photovoltaic junctions, J. Mater. Sci. Mater. Electron. **11**, 525 (2000).

[24] N. Yao, *Focused Ion Beam Systems* (Cambridge University Press, Cambridge, UK, 2010).

[25] A. A. Taylor, J. D. Major, G. Kartopu, D. Lamb, J. Duenow, R. G. Dhere, X. Maeder, S. J. C. Irvine, K. Durose, and B. G. Mendis, A comparative study of microstructural stability and sulphur diffusion in CdS/CdTe photovoltaic devices, Sol. Energy Mater. Sol. Cells **141**, 341 (2015).

[26] X. Liu, A. Abbas, M. Togay, V. Kornienko, R. Greenhalgh, K. Curson, J. Bowers, K. Bath, M. Walls, E. Bastola, G. Barros-King, A. B. Phillips, and M. J. Heben, The effect of remnant CdSe layers on the performance of CdSeTe/CdTe photovoltaic devices, Sol. Energy Mater. Sol. Cells **267**, 112717 (2024).

[27] See the Supplemental Material at http://link.aps.org/supplemental/10.1103/PRXEnergy.3.023002 for (i) device performance parameters, (ii) STEM EDX Se interdiffusion profiles, and (iii) curtaining effect around grain boundary porosity in the 400 nm CdSe sample.

[28] X. Zheng, E. Colegrove, J. N. Duenow, J. Moseley, and W. K. Metzger, Roles of bandgrading, lifetime, band alignment, and carrier concentration in high-efficiency CdSeTe solar cells, J. Appl. Phys. **128**, 053102 (2020).

[29] G. T. Koishiyev, J. R. Sites, S. S. Kulkarni, and N. G. Dhere, in *2008 33rd IEEE Photovoltaic Specialists Conference (PVSC)* (San Diego, CA, USA, 2008), pp. 1.

[30] J. Lee, N. C. Giles, D. Rajavel, and C. J. Summers, Room-temperature band-edge photoluminescence from cadmium telluride, Phys. Rev. B **49**, 1668 (1994).

[31] B. G. Mendis, Planck's generalised radiation law and its implications for cathodoluminescence spectra, Ultramicroscopy **204**, 73 (2019).

[32] V. Consonni, G. Feuillet, and S. Renet, Spectroscopic analysis of defects in chlorine doped polycrystalline CdTe, J. Appl. Phys. **99**, 053502 (2006).

[33] B. G. Mendis, D. Gachet, J. D. Major, and K. Durose, Long lifetime hole traps at grain boundaries in CdTe thin-film photovoltaics, Phys. Rev. Lett. **115**, 218701 (2015).

[34] I. Pelant and J. Valenta, *Luminescence Spectroscopy of Semiconductors* (Oxford University Press, Oxford, 2012).

[35] P. B. Hirsch, A. Howie, R. B. Nicholson, D. W. Pashley, and M. J. Whelan, *Electron Microscopy of Thin Crystals* (Butterworths, Great Britain, 1965).

[36] R. A. Lomas-Zapata, A. W. Prior, and B. G. Mendis, A simulation study of the role of anisotropic charge transport and grain boundary recombination in thin-film Sb_2Se_3 photovoltaics, Sol. Energy **264**, 112054 (2023).

[37] A. Romeo, D. L. BÓŞtzner, H. Zogg, and A. N. Tiwari, Recrystallization in CdTe/CdS, Thin Solid Films **361–362**, 420 (2000).

[38] H. R. Moutinho, M. M. Al-Jassim, D. H. Levi, P. C. Dippo, and L. L. Kazmerski, Effects of $CdCl_2$ treatment on the recrystallization and electro-optical properties of CdTe thin films, J. Vac. Sci. Technol., A **16**, 1251 (1998).

[39] H. R. Moutinho, F. S. Hasoon, F. Abulfotuh, and L. L. Kazmerski, Investigation of polycrystalline CdTe thin films deposited by physical vapor deposition, close-spaced sublimation, and sputtering, J. Vac. Sci. Technol., A **13**, 2877 (1995).

[40] M. Prutton, *Introduction to Surface Physics* (Oxford University Press, New York, 1994).

[41] D. A. Porter, K. E. Easterling, and M. Y. Sherif, *Phase Transformations in Metals and Alloys*, 3rd ed. (CRC Press, Florida, 2009).

[42] T. Gladman, On the theory of the effect of precipitate particles on grain growth in metals, Proc. R. Soc. London, Ser. A **294**, 298 (1966).